



A noise removal algorithm based on adaptive elevation difference thresholding for ICESat-2 photon-counting data

Bikang Wang^{a,b}, Yi Ma^{a,b,*}, Jingyu Zhang^{a,b}, Huanwei Zhang^{a,b}, Haitian Zhu^c, Zihao Leng^{a,b,d}, Xuechun Zhang^{a,b,d}, Aijun Cui^{a,b,e}

^a First Institute of Oceanography, Ministry of Natural Resources, Qingdao 266061, China

^b Technology Innovation Center for Ocean Telemetry, Ministry of Natural Resources, Qingdao 266061, China

^c National Satellite Ocean Application Service, Beijing 100089, China

^d College of Oceanography and Space Informatics, China University of Petroleum, Qingdao 266500, China

^e College of Geodesy and Geomatics, Shandong University of Science and Technology, Qingdao 266590, China

ARTICLE INFO

Keywords:

ICESat-2 ATL03 data

Photon noise removal

Elevation difference histogram

Water depth

ABSTRACT

Ice, Cloud, and Land Elevation Satellite-2 (ICESat-2) has shown great potential for near-shore bathymetry. Unavoidably, the photon data acquired has a lot of noise. In order to remove noise more accurately, a photon denoising algorithm based on adaptive elevation difference thresholding (AEDTA) is proposed under the assumption that the terrain is continuously changing. The algorithm uses a Gaussian function obtained by fitting an elevation histogram to ICESat-2 data for the extraction of underwater photons. Repeatedly count the elevation difference histogram of underwater photons and adaptively determine the threshold. And the final denoised underwater signal photons are obtained. Compared with the conventional clustering method of ordering points to identify the clustering structure (OPTICS), our algorithm achieves better photon detection results for underwater topography for different densities of ICESat-2 data and has the advantage of parameter adaption without human intervention. ICESat-2 data from Ganquan Island, Dongdao Island and Oahu Island were selected for testing, and the ICESat-2 bathymetry results calculated by the algorithm were compared with *in situ* bathymetry data to assess the reliability and accuracy of the proposed denoising algorithm. The results show that the MAE of the bathymetry results calculated using the ICESat-2 signal photon data extracted by the method ranged from 0.54 to 1.57 m and the RMSE ranged from 0.64 to 1.74 m in different seas. The algorithm can provide high quality denoised data for bathymetric mapping around coastal areas and islands. Meanwhile, the AEDTA algorithm also has a good denoising effect on terrestrial photons, and the effect of cloud shading on the Gaussian fit analysis of ICESat-2 data cannot be ignored.

1. Introduction

Water depth is an important basic data for marine resources development, marine environmental protection and marine shipping (Yi et al., 2018). The measurement methods of bathymetric data include shipborne sonar, airborne lidar and spaceborne lidar. Bathymetric data acquired by shipborne sonar and airborne lidar have the advantage of being highly accurate (cm level), spatially dense and less noisy (Costa et al., 2009). But shipboard sonar and airborne lidar are time consuming, labor intensive and expensive, which can only obtain bathymetry data for a small sea area during a single flight or voyage. Spaceborne lidar brings a novel opportunity for nearshore bathymetry which can obtain

water depth data (dm-level accuracy) in areas that are difficult for ships and aircraft to reach (Albright and Glennie, 2021; Caballero and Stumpf, 2019; Rannadal et al., 2021). But there is a lot of noise in the photon data obtained from the spaceborne lidar. And photon denoising is a necessary process.

ICESat-2 equipped with the Advanced Topographic Laser Altimeter System (ATLAS) was launched in September 2018 (Hsu et al., 2021). ATLAS instrument transmits micro-pulses with a pulse energy of 0.2 mJ–1.2 mJ at a high pulse repetition frequency of 10 kHz. However, it receives only several returned photons (the number of the returned photons is about 0.05–1 per pulse at sea surface). Each transmitted laser pulse is split into three pairs of laser beams, each with a 4:1 energy ratio

* Corresponding author at: First Institute of Oceanography, Ministry of Natural Resources, Qingdao 266061, China.

E-mail address: mayimail@fio.org.cn (Y. Ma).

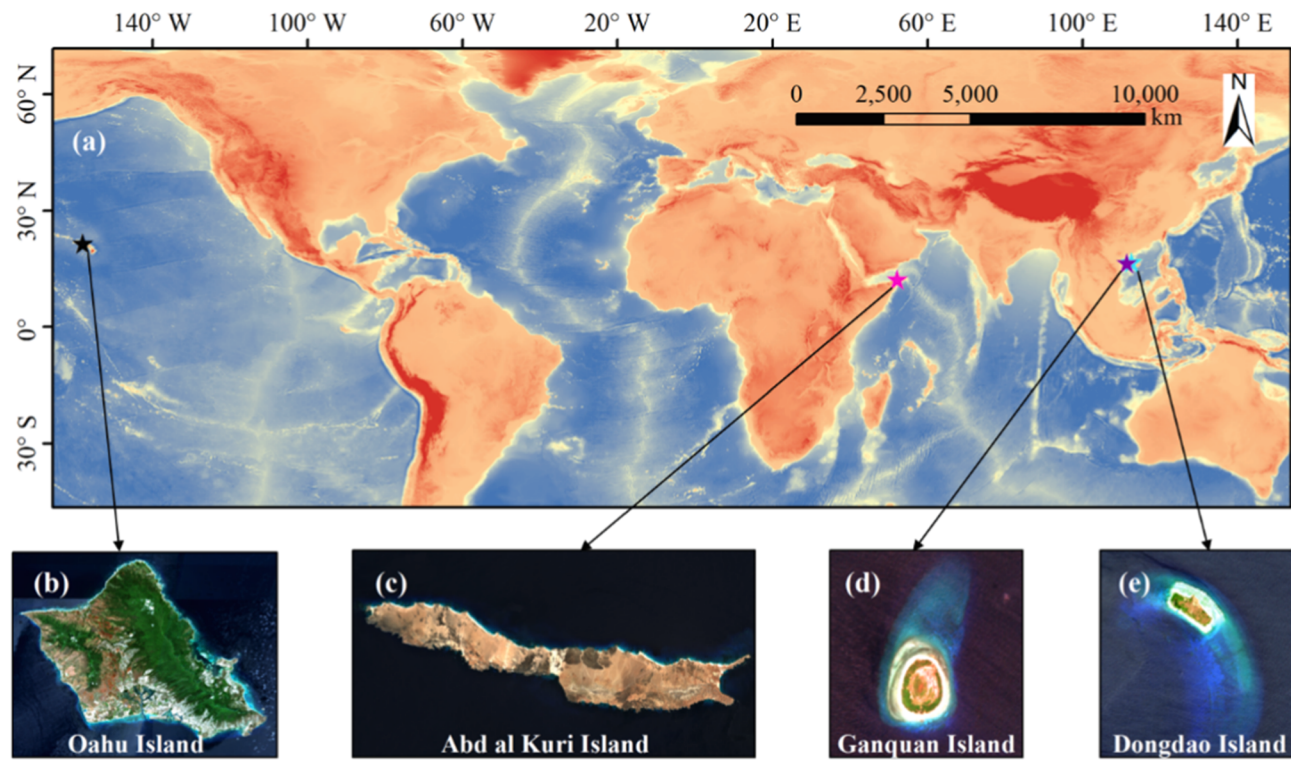


Fig. 1. The locations of Oahu Island (b), Abd al Kuri Island (c), Ganquan Island (d), and Dongdao Island (e) in the Global Relief Model (a).

between the strong and weak beams. The interval between three pairs of beams is 3.3 km, and the interval between each pair of beams is 90 m (Markus et al., 2017). The flight height of ICESat-2 is 500 km. A laser pulse with a wavelength of 532 nm is generated every 0.7 m along the ground track direction (Thomas et al., 2022). The ATLAS instrument uses photon-counting techniques to measure the time it takes for a photon to travel from ATLAS to earth and back, and record the latitude and longitude of each photon. The laser pulse wavelength of 532 nm has an ability of water penetration (Li et al., 2019; Zhang et al., 2021; Zhang et al., 2022a).

Sunlight also contains green light with a wavelength of 532 nm, the solar background photons generated by the 532 nm green light in this part of sunlight are reflected into ATLAS and recorded by the receiving equipment, so the noise number of daytime data is larger than that of nighttime data. When an ATLAS photon touches an object, it returns to the ATLAS instrument and is recorded as a photon event. These objects may be terrain, trees, clouds, underwater occlusions, etc. We need to remove these non-terrain photons through a denoising algorithm to get accurate elevation data (Magruder and Brunt, 2018). According to the characteristics of dense signal photons and sparse noise photons, the current photon denoising algorithms mainly focus on using the parameter density as a threshold to distinguish signal photons from noise photons (Xie et al., 2021; Xie et al., 2022). And how to determine the search radius and the number of neighborhood points becomes the key to the density-based denoising algorithm. Regarding how to determine the search radius, relevant scholars have developed different shapes of denoising neighborhoods such as circle, ellipse, and rectangle, and determined their size according to terrain characteristics (Chen et al., 2021; Yang et al., 2022; Zhang et al., 2022). As for the number of neighborhood points, the current main method is to manually specify the number of neighborhood points based on experience. Relevant scholars have developed segmentation in the direction of elevation according to the feature that the number of photon decays with depth and adaptively determine the threshold of photon count for each segment (Surisetty et al., 2022). At present, the commonly used density-based denoising methods are DBSCAN (Density-Based Spatial Clustering of

Applications with Noise) (Bacalhau et al., 2022; Ma et al., 2020; Wang et al., 2022; Xie et al., 2021; Xu et al., 2022) and OPTICS (Zhu et al., 2021). Both DBSCAN (Ester et al., 1996) and OPTICS (Ankerst et al., 2008) methods are density-based clustering algorithms, and OPTICS can cluster clusters of arbitrary density. These algorithms can be found in python's sklearn library (Pedregosa et al., 2011), based on which improvements can be made with either manually specified parameters or adaptively determined parameters. For the noise photons that cannot be removed by above algorithm, it is often removed by manual editing (Babbel et al., 2021; Thomas et al., 2021). The DRAGANN (Differential, Regressive, and Gaussian Adaptive Nearest Neighbor) algorithm is mainly used for terrestrial photon denoising, which classifies photons into ground photons and canopy photons (NASA, 2019; Neuenschwander and Katherine, 2018). The DRAGANN algorithm uses an iterative Gaussian filter based on the histogram of each photon to filter the noise. The histogram of each photon's nearest neighbor, where the ten largest Gaussian components are iteratively removed (Lin et al., 2020). Although these methods can achieve good denoising after the parameters are adjusted properly, it is time-consuming and labor-intensive for those who only want to extract the elevation signal photons. And when there is a large number of noise photons in the original data, a single density threshold is not ideal for detecting underwater terrain points.

In this paper, a noise removal algorithm based on adaptive elevation difference thresholding for ICESat-2 data (AEDTA) is developed which uses the elevation difference as the threshold and can adaptively determine the threshold according to the characteristics of the data. To verify the reliability of the algorithm, Ganquan Island, Dongdao Island and Oahu Island with *in situ* bathymetry data were selected as the study areas. The error between *in situ* bathymetry data and ICESat-2 bathymetry data was also calculated. Meanwhile, the denoising results of the AEDTA algorithms and the OPTICS algorithms are compared. In the discussion, the denoising processes of the algorithm and the denoising effect of terrestrial photons are analyzed by using Abd al Kuri Island ICESat-2 data. We also discuss the Gaussian fitting analysis of cloud-shaded ICESat-2 data, the feasibility of using elevation difference as a threshold, and the adaptive parameters of the denoising algorithm.

Table 1

Detailed information about the study areas.

Island Name	Latitude range	Longitude range	Area
Ganquan Island	16.5004°-16.5204°N	111.5803°-111.5896°E	0.3 km ²
	16.6194°-16.6952°N	112.6922°-112.7729°E	1.7 km ²
Dongdao Island	21.2420°-21.7158°N	158.2908°-157.6371°W	1574 km ²
	12.1472°-12.2457°N	52.0628°-52.3938°E	133 km ²

2. Data and methods

2.1. Study area

In this study, four study areas are involved. As shown in Fig. 1, ICESat-2 data for different bathymetric ranges were selected on the islands of Ganquan, Dongdao, Oahu and Abd al Kuri. They have different topographical features underwater. The ICESat-2 bathymetry data was compared with *in situ* bathymetry data from Ganquan Island, Dongdao Island and Oahu Island. Due to the unavailability of *in situ* bathymetry data for Abd al Kuri Island, the denoising effect of the algorithm in this paper is only visually analyzed in the discussion.

Ganquan Island is located in the western part of Yongle Atoll, which is situated in the western part of China's Xisha Islands. Dongdao is the second largest island in China's Xisha Islands and lies to the east of the Xuande Islands. Oahu island is positioned in the northwestern part of the Hawaiian archipelago. And Oahu Island is the third largest island in the Hawaiian archipelago in the USA, which is located in the central Pacific Ocean. Abd al Kuri Island sits in the western part of the Socotra Islands. Table 1 shows more detailed information about the study area.

2.2. Data

2.2.1. ICESat-2 ATL03 data

Considering the location of the validation data and the quality of the ICESat-2 data in the study area, six tracks of ICESat-2 ATL03 data were selected for the experiment as shown in Table 2. The ATL03 datasets are free from <https://openaltimetry.org/data/icesat2/>. The ATL03 raw data photons were used (including all photons with confidence from 0 to 4). And the details of the ICESat-2 ATL03 data are given in Table 2.

To verify the reliability of the algorithm in this paper, ICESat-2 ATL03 data were selected which located in Ganquan Island (Fig. 2(a)), Dongdao Island (Fig. 2(b)), Oahu Island (Fig. 2(c)), and Abd al Kuri Island (Fig. 2(d)). ATL03 data is global geolocation photon data, including the longitude, latitude, elevation and confidence of each photon. And the terrestrial reference system is WGS-84 ellipsoid (ITRF2014 reference frame). These data are stored in the group/gtx/heights. An ATL03 data file contains photon data from six strips (gt1l, gt1r, gt2l, gt2r, gt3l, gt3r, where l and r represent left and right respectively), but not all six strips can be distributed along shallow coastal areas or contain underwater topographic photons due to the cross-track distance and weak laser beam. Therefore, data for which signal photons can be visually detected should be given priority as research data in the initial screening. They are then denoised and

underwater topographic photons can be extracted.

2.2.2. In situ bathymetry data

In this paper, the validation processing used *in situ* bathymetry data which was obtained from the National Natural Science Foundation of China (Fig. 3). The verification data of Ganquan Island is the shallow water depth data obtained by the lidar sounding device Aquarius (Optech Company, Canada) in 2013. The working band of this device is the blue-green band (532 nm), and the sounding error RMSE is 0.3 m. The verification data of Dongdao Island were measured by the single-beam echosounders (SBES) in 2011, and the depth error is 0.01 m. The verification data for Oahu Island was collected by the Scanning Hydrographic Operational Airborne Lidar Survey (SHOALS) in 2011, and the depth error was 0.15 m. Because the location of the *in situ* bathymetry does not correspond exactly to the icesat-2 bathymetry, a raster map is generated using kriging interpolation of the *in situ* bathymetry points, and the pixel values of the raster map are extracted based on the latitude and longitude of the icesat-2 bathymetry points for comparison.

2.3. Methods

2.3.1. Overall workflow

The distribution characteristics of photons on land, sea surface and underwater are different, so we should distinguish raw photon data into above water photons, sea surface photons, and under water photons. And the threshold for classifying photons is the elevation range of photons on the sea surface. Since there are a large number of noise photons in the original photon data, it is necessary to remove the noise photons from the raw photon data according to the characteristics of each type of photon. In this paper, combined with the principle of continuous change of terrain, the elevation difference is used as a threshold to distinguish between noise photons and signal photons. Furthermore, we propose a denoising algorithm that adaptively determines the threshold of the elevation difference according to the height difference histogram. A flow chart of our denoising algorithm can be learned in Fig. 4.

First, the method uses the elevation with the highest frequency in the elevation histogram as the sea surface height. And the photons that meet the 5 m neighborhood of sea surface height are selected for Gaussian fitting. Then distinguish above water photons, sea surface photons and under water photons using the mean and standard deviation in the fitted Gaussian function. Second, count the histogram for the elevation difference of underwater photons. The horizontal coordinate of the elevation difference histogram is the elevation difference of all underwater adjacent two photons divided into 100 segments (empirically specified) and the vertical coordinate is the frequency of all elevation differences occurring within each segment. Then, the starting coordinates of each section of elevation difference are chosen as the x-value of the attenuation model, and the frequency of each section of elevation difference is the y-value, and the attenuation model is fitted. To remove the noise photons which have a large elevation difference in neighboring photons but a small number. And the problem is transformed to make the constant term c in the fitted attenuation model close to 0. Therefore, the value of y representing frequency is looped. Select

Table 2

Detailed information of the ICESat-2 ATL03 data.

Location	Data name	Date	Time(Local)	Track ID
Ganquan Island	ATL03_20220317202009_13071401_005_01.h5	2022-03-17	20:20	gt2l
Dong dao Island	ATL03_20181116062310_07430101_005_01.h5	2018-11-16	06:23	gt3r
Oahu Island	ATL03_20220304145339_11051401_005_01.h5	2022-03-04	14:53	gt1l
Oahu Island	ATL03_20181209231549_11050101_005_01.h5	2018-12-09	23:15	gt2r
Oahu Island	ATL03_20220109053856_02741407_005_01.h5	2022-01-09	05:38	gt1l
Abd al Kuri Island	ATL03_20201019125412_03870907_005_01.h5	2020-10-19	12:54	gt2l

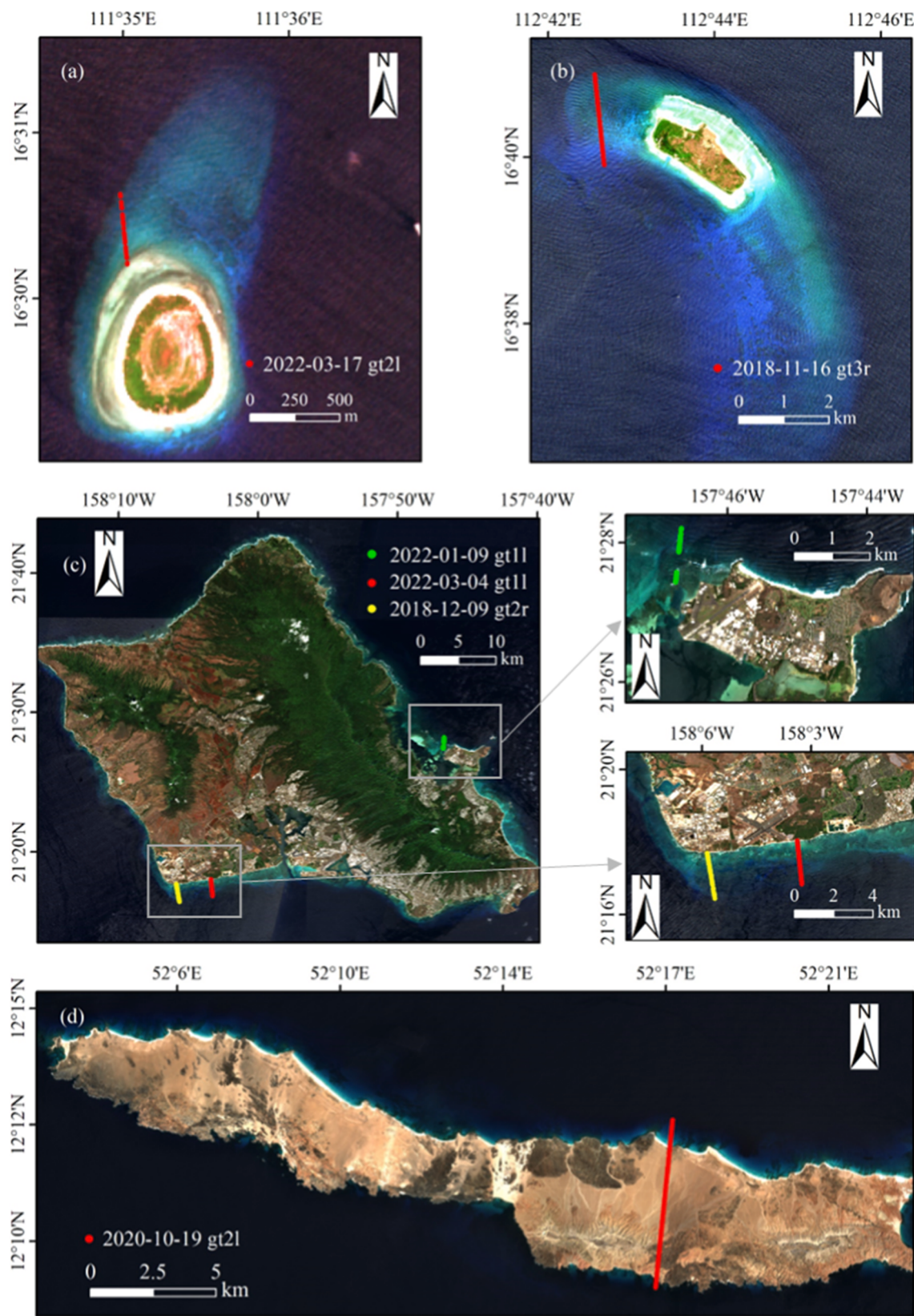


Fig. 2. Sentinel-2A Satellite true color images of Ganquan Island (a), Dong dao Island (b), Oahu Island(c), and Abdu al Kuri Island (d), the dotted data in the figure shows the location of ICESat-2 ATL03 data in each study area.

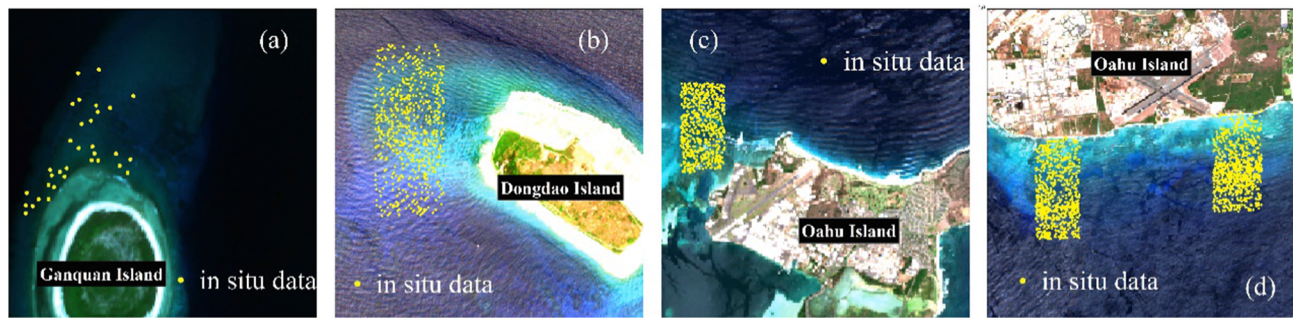


Fig. 3. The locations of the *in situ* bathymetry data.

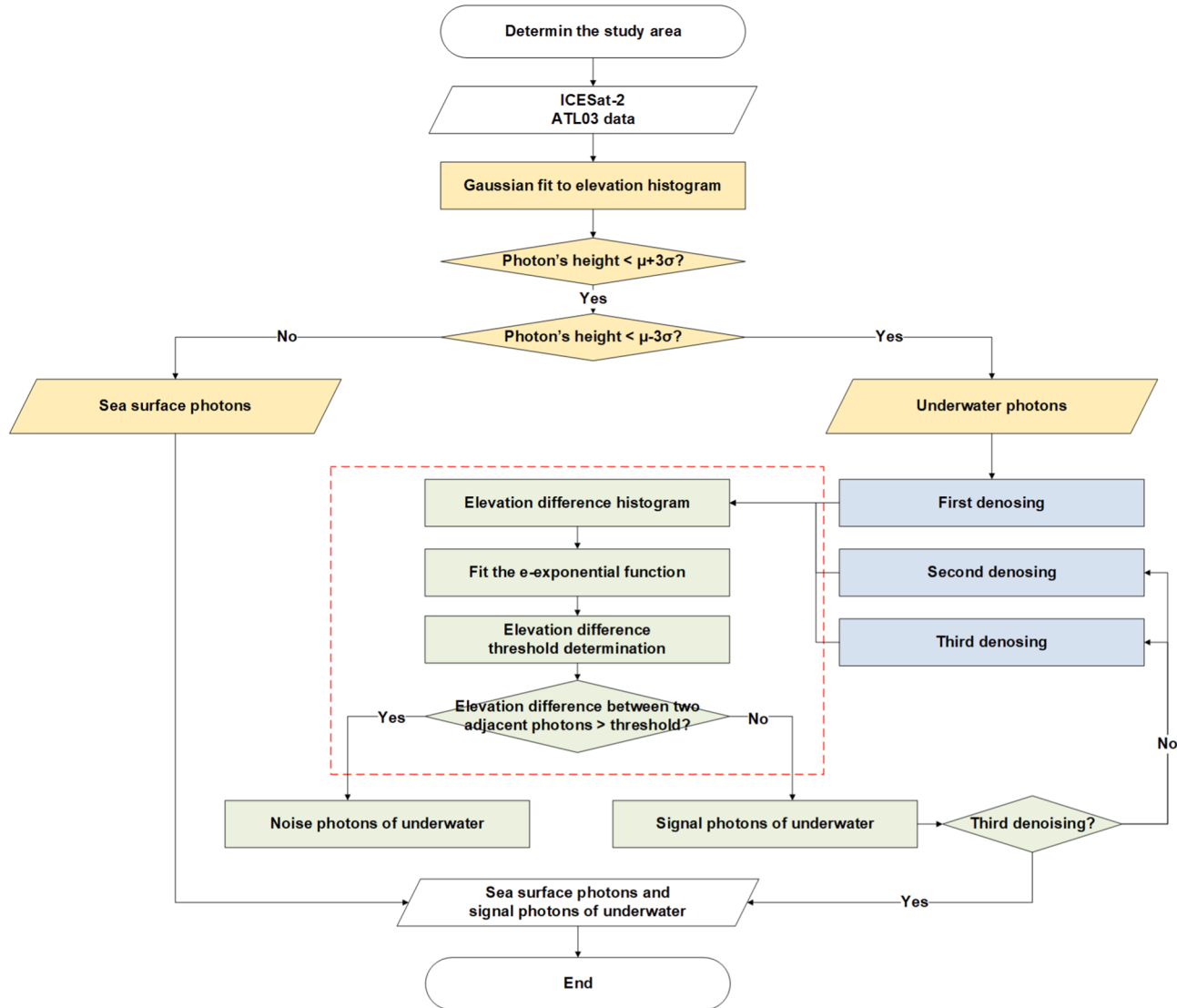


Fig. 4. Flowchart of the proposed algorithm for photon denoising. AEDTA = the noise removal algorithm based on adaptive elevation difference thresholding.

the elevation difference corresponding to the y value that satisfies the $|y - c - 0| < 10^{-3}$ condition as the threshold for the first denoising. And divide photons into signal and noise photons based on this threshold. When the difference in elevation between two adjacent photons is greater than this threshold, these two adjacent photons are marked as noise photons, otherwise, they are marked as signal photons. Last, repeat the second step, which performs the second denoising using the photons marked as a signal by the first denoising and perform the third denoising

using the photons marked as a signal by the second denoising. Then we can get the final denoising result. For terrestrial photons, denoising can also be done according to the above method. In this paper, we focus on the denoising of underwater photons, and in the discussion, we also analyze the effectiveness of the proposed algorithm on the denoising of terrestrial photons. The advantage of this method is that it does not require any manual determination of parameters and adapts to the characteristics of ICESat-2 ATL03 data itself to derive a threshold value

that is appropriate for the data itself to distinguish between signal and noise.

2.3.2. Detailed workflow

The characteristic of photon-counting for ATLAS instrument is that high frequency pulses are emitted while only several returning photons are received. Therefore, the photon data acquired by the ATLAS instrument contains not only signal photons but also a large number of noise photons. Effectively removing noise is a major obstacle to applying ICESat-2 data. The ATL03 data records terrain, trees, cloud cover, underwater obstacles, etc. For different applications we need to keep as signal photon objects also differ. Since the distribution characteristics of land photons, sea surface photons and underwater photons are different, it is necessary to distinguish these three types of photons and denoise them according to their characteristics. When the laser penetrates the water, the path of the photons is shifted due to the refraction effect, so it is necessary to correct the refraction of the underwater photons.

(Step1) identify and separate the photons of above water, water surface, and under water

Due to the different distribution characteristics of photons of above water, water surface, and under water, and the refraction effect of photons penetrating water, it is necessary to classify the original photons and denoise each type of photon separately to achieve a good denoising effect. And the critical elevation points for distinguishing these three types of photons are the upper and lower elevation bounds of photons on the water surface. Since only a few photons will penetrate the water surface and most of the photons will stay on the sea surface, the sea surface elevation can be determined according to the elevation with the highest frequency in the elevation histogram.

By counting the elevation histograms of all the photons, the elevation with the highest frequency in the elevation histogram is chosen as the sea surface height. If a Gaussian function is fitted to the elevation histograms of all photons, it is found that the number of Gaussian peaks could not be determined. Photon groups formed by the influence of clouds, relatively flat terrain and underwater terrain points may all form Gaussian peaks, resulting in the existence of multiple Gaussian peaks. Therefore, the photon data of Gaussian fitting should be limited to a certain range. According to the assumption that the water surface elevation does not fluctuate more than 5 m, we filter out photons that satisfy the condition that the water surface elevation value fluctuates within 5 m from all photons. And by counting the elevation histogram for this part of the photons, it is observed that the elevations of this part of the photons exhibit a good single-peaked Gaussian distribution. The reason for the Gaussian distribution of photons on the sea surface is that the wave undulations revolve around a fixed value, most of the photons will be concentrated at this fixed value, and the number that deviates from this fixed value is smaller. First, perform Gaussian function fitting according to Eq. (1). Then the mean value and three times the standard deviation in the fitted Gaussian function are used as the threshold to accurately separate terrestrial photons, sea surface photons, and underwater photons (Eq. (2)). While the Gaussian distribution on probability

theory and mathematical statistics considers the data outside three times the standard deviation as noise, while the data within three times the standard deviation as signal. There is no need to denoise the water surface photons, since they are already limited to a reasonable and small range when using the mean value and three times the standard deviation of the Gaussian function, photons within this range can be considered as water surface photons. Eq. (1) is the formula used to fit the Gaussian to the elevation histogram. Eq. (2) is the method to classify photons according to the threshold.

$$f = a \times \exp \left\{ -\frac{(x - \mu)^2}{2 \times \sigma^2} \right\} \quad (1)$$

$$\begin{cases} h_{ph} > \mu + 3 \times \sigma, \text{Photons of above water} \\ \mu - 3 \times \sigma < h_{ph} < \mu + 3 \times \sigma, \text{Photons of water surface} \\ h_{ph} < \mu - 3 \times \sigma, \text{Photons of under water} \end{cases} \quad (2)$$

where a is the amplitude of the fitted Gaussian function, μ is the horizontal coordinate of the fitted Gaussian peak, σ is the width of the fitted Gaussian peak, h_{ph} is the height of each photon, relative to the WGS-84 ellipsoid.

(Step 2) denoising under water photons

Since the study area is the shallow sea, it is assumed that the underwater terrain changes continuously and gently, that is, the elevation difference between two adjacent photons will not be greater than a certain threshold. The penetration of laser is limited, and the maximum sounding range in clean water is about 50 m. In most cases, the sounding range is about 20 m, and the terrain fluctuations in this water depth range are relatively gentle.

And how to determine the threshold value of the elevation difference between two adjacent photons for detecting underwater terrain photons becomes the key of this algorithm. First, calculate the elevation difference of adjacent photons according to Eq. (3) and count the histogram of the elevation difference. Second, after analyzing the histogram of the elevation difference between two adjacent under water photons, it exhibits an e-exponential decay distribution. It is necessary to convert the y-axis of the histogram from probability density to frequency according to Eq. (4) and Eq. (5). Noise photons are randomly distributed, so their elevation difference distribution is not centralized. While the distribution of signal photons satisfies the continuity assumption, so its elevation difference distribution is centralized. Under the assumption of slow changes in underwater topography, the number of photons with a smaller elevation difference is higher. And the elevation difference histogram can be fitted using the attenuation model (Eq. (6)). Eq. (4) and Eq. (5) are the conversion relationship between frequency and probability, Eq. (6) is the e-exponential decay formula for fitting the elevation difference histogram

$$h_{diff} = |h_{i+1} - h_i|, i = 1, 2, \dots, N \quad (3)$$

$$p = \frac{n}{(N \times bw)} \quad (4)$$

$$f = p \times bw \quad (5)$$

$$y = a * \exp\{-b * x\} + c \quad (6)$$

where h_{diff} is the elevation difference of two adjacent photons, h_i is the elevation of the i -th photon, N is the total number of all photons, n is the count of each elevation difference, bw is the width of the elevation difference histogram segments, p is the vertical coordinate of the elevation difference histogram, f is the frequency of occurrence of elevation difference, a is the amplitude of the fitted attenuation model, b is the decay rate of the attenuation model, c is the constant term of the attenuation model.

Our aim is to mark photons with elevation differences greater than a certain threshold as noise and remove them. Therefore, the problem can be transformed into making the constant term c in the fitted attenuation

Table 3

Accuracy evaluation of ICESat-2 bathymetry data and *in situ* bathymetry data.

Location	Data name	Depth range (m)	MAE (m)	RMSE (m)	MRE (%)	R ²
Ganquan Island	ATL03_20220317	0–10	0.63	0.97	11.1	0.85
Dongdao Island	ATL03_20181116	7–28	1.57	1.74	12.1	0.95
Oahu Island	ATL03_20220304	1–22	0.81	0.94	20.3	0.99
Oahu Island	ATL03_20181209	1–25	0.56	0.77	12.6	0.98
Oahu Island	ATL03_20220109	1–15	0.54	0.64	12.3	0.99

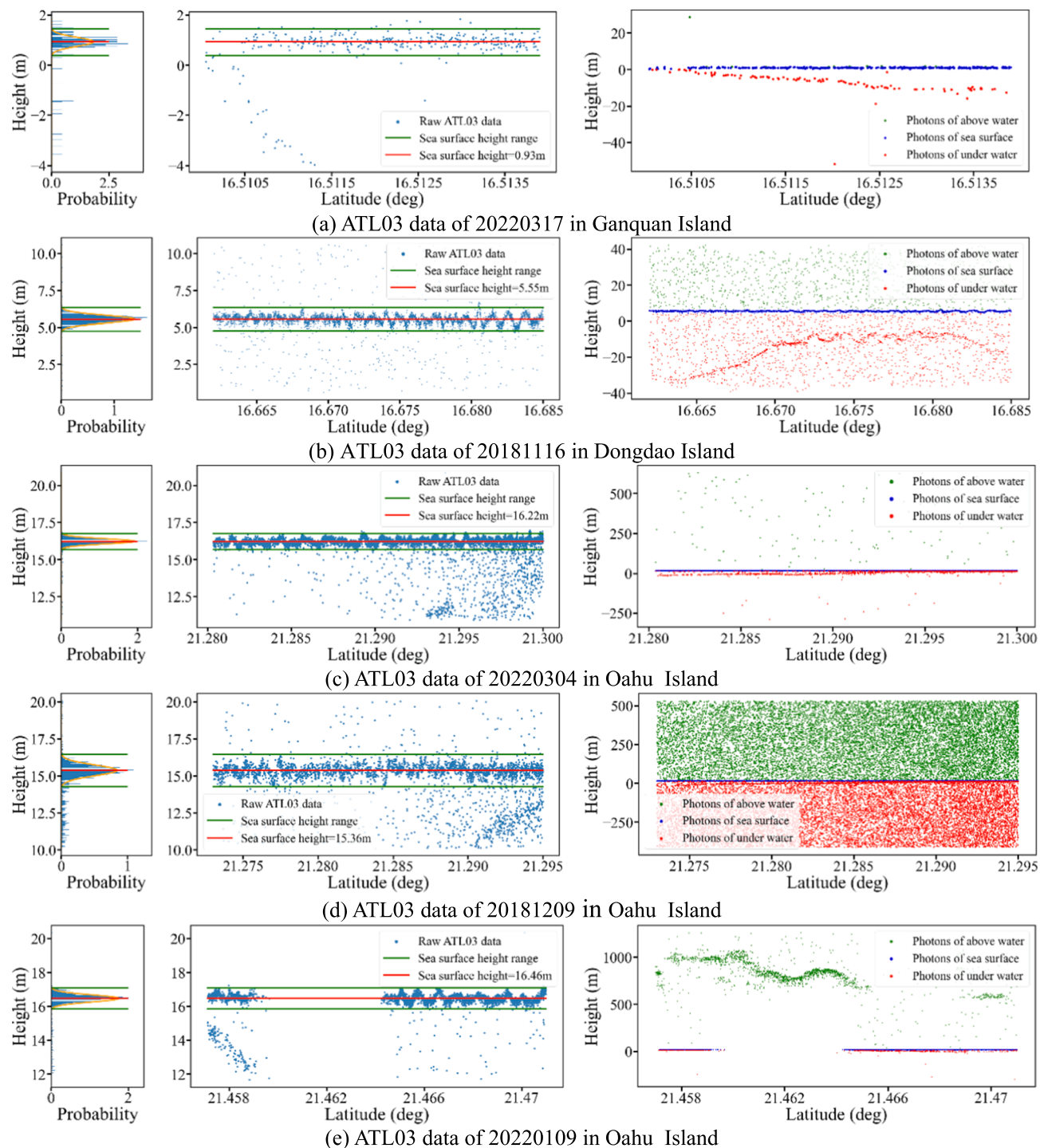


Fig. 5. The elevation range of sea surface photon and the classification results of photon, where images (a)-(e) represent ICESat-2 data for different orbits. The images in the left column show the results of a Gaussian fit to the elevation histogram of photons within five meters of sea surface height. The images in the middle column show the sea surface height value (red line) and the range of elevation values for sea surface photons (green line). And the image in the right column shows the result of classifying the photons according to the threshold, the green dots is the photons of above water, the blue dots is the photons of sea surface and the red dots are the photons of under water. (For interpretation of the references to color in this figure legend, the reader is referred to the web version of this article.)

model as close to zero as possible. The elevation difference corresponding to the maximum of the frequency y values satisfying the condition of $|y - c - 0| < 10^{-3}$ is used as the elevation difference threshold for the first denoising. And classify the photons into signal photons and noise photons according to this threshold.

To avoid that several adjacent photons are all noise, count the elevation differences histogram for the signal photons obtained by the first denoising. If the elevation difference between two adjacent photons

at the second count is too large, it can also be considered as noise removal as well. Repeat the above operation for the result of the second denoising for the third denoising.

From Table 3 in Section 4.4, We can see that the value of the constant term c is getting smaller and the amplitude term is getting larger. Thus, the purpose of denoising is achieved.

(Step3) refraction correction and the calculation of water depth values.

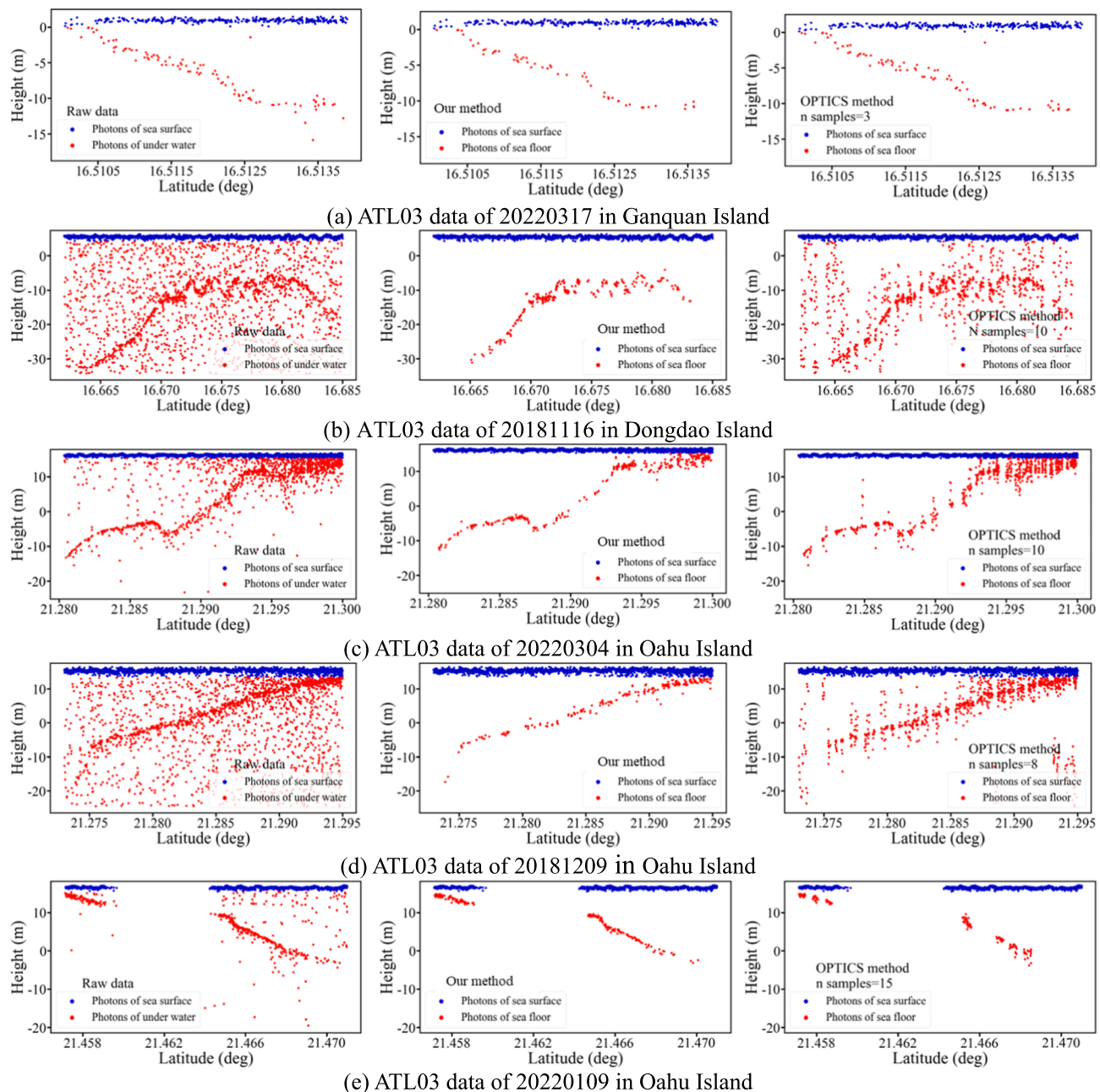


Fig. 6. Comparison of the signal photon extraction of under water between our method and OPTICS method. And images in each row represent ICESat-2 data for one orbit. The graphs in the left column show the raw ICESat-2 ATL03 data. The graphs in the middle column show the denoising results of the method in this paper. The graphs in the right column show the denoising results of the method in OPTICS. The blue dots are the photons of sea surface, the red dots are the photons of under water. (For interpretation of the references to color in this figure legend, the reader is referred to the web version of this article.)

Since the horizontal offset in longitude and latitude without refraction correction is only 9 cm when the water depth is 30 m ($0.003 \times D = 0.003 \times 30 = 9\text{cm}$) (Parrish et al., 2019), the horizontal offset is negligible. A refraction correction and calculation of water depth can be done according to Eqs. (7)-(9).

$$D = ssh - h_{ph} \quad (7)$$

$$h_{ph_cor} = h_{ph} + 0.25416 \times D \quad (8)$$

$$D_{cor} = seasurfaceheight - h_{ph_cor} \quad (9)$$

where D is the water depth value before refraction correction, h_{ph} is the elevation value of each underwater photon. h_{ph_cor} is the elevation value of each underwater photon after refraction correction. ssh is the

value of sea surface elevation. D_{cor} is the water depth value after refraction correction.

2.3.3. Evaluation methodology

For ICESat-2 ATL03 data in Table 1, the de-noised and refraction-corrected data are compared with the *in-situ* bathymetry data, we can calculate the mean absolute error (MAE), root mean square error (RMSE), mean relative error (MRE), and coefficient of determination R^2 according to Eqs. (10)-(13). The RMSE is more susceptible to outliers than the MAE and RMSE are calculated to help detect the presence of large and uncommon outlier errors.

$$MAE = \frac{1}{n} \sum_{i=1}^n |y_i - \hat{y}_i| \quad (10)$$

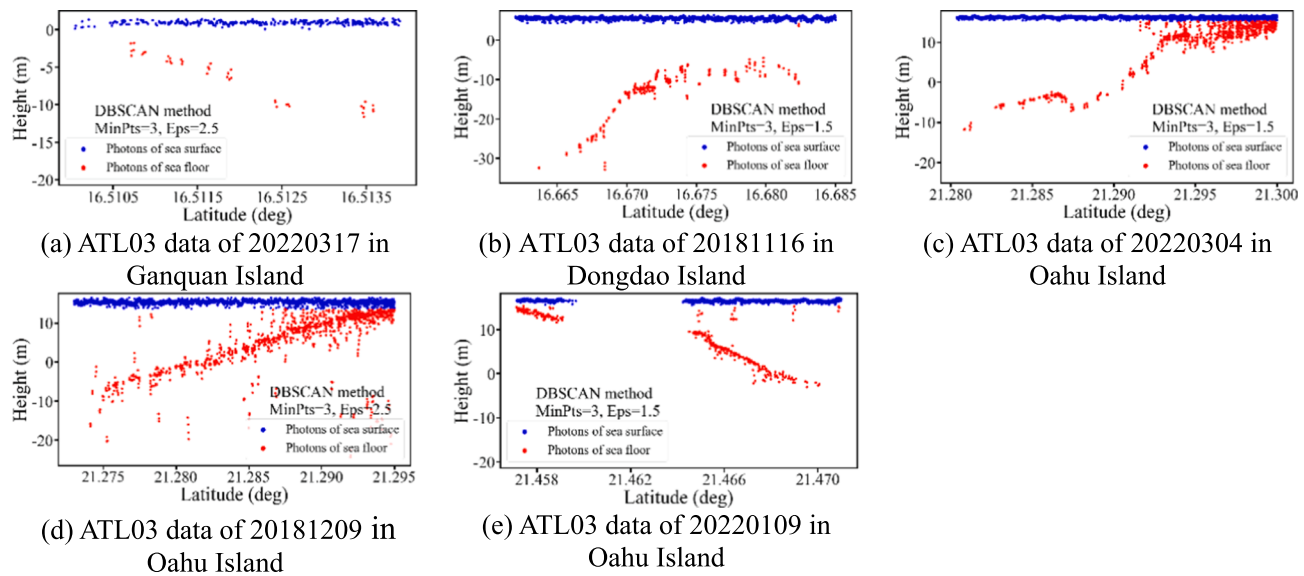


Fig. 7. The denoising results of the method in DBSCAN.

$$RMSE = \sqrt{\frac{1}{n} \sum_{i=1}^n (y_i - \hat{y}_i)^2} \quad (11)$$

$$MRE = \frac{1}{n} \sum_{i=1}^n \left| \frac{y_i - \hat{y}_i}{\hat{y}_i} \right| \quad (12)$$

$$R^2 = 1 - \frac{\sum_{i=1}^n (y_i - \hat{y}_i)^2}{\sum_{i=1}^n (y_i - \frac{1}{n} \sum_{i=1}^n y_i)^2} \quad (13)$$

where y_i is the water depth calculated by ICESat-2 data, \hat{y}_i is the *in situ* bathymetry data, n is the total number of water depth.

3. Results and analysis

3.1. Classification of photons

Following the method in step 1 in section 2.3.2, the photon classification results can be derived as shown in Fig. 5 (a)-(e). We can find that different types of photons have different characteristics. Photons of above water show a random distribution under cloud-free conditions and impenetrability in the presence of thick clouds. Photons of sea surface show aggregated distribution characteristics and the elevation fluctuations are limited to a certain range. The signal photons in underwater photons show an aggregated distribution, and the elevation difference between two adjacent signal photons is small. In all figures in this paper, Height on the y-axis is the height of each photon relative to the WGS-84 ellipsoid.

3.2. Visual comparison for denoising results

Comparison of the signal photon extraction of underwater between our method and OPTICS method. The algorithm of OPTICS is a density-based denoising method. And it can separate signal photons and noise photons according to the set density threshold. However, different ICESat-2 data have different characteristics, OPTICS method needs to try one by one to find the most suitable parameter of density threshold for this data. And it takes a lot of unnecessary time to adjust the parameters.

As the graphs in the left column of Fig. 5 show, it can find that for ICESat-2 data with different density noise distribution, the number of photons decreases with depth. The threshold value needs to be determined individually for each track of ICESat-2 data.

Following the method in step 1 and 2 in section 2.3.2, it can obtain the graphs as shown in the middle column of Fig. 6. The method in this paper removes most of the noise photons and avoids the tediousness of manual parameter adjustment.

In this paper, by adjusting the parameter of n samples to 0, 1, 2, ..., 30 one by one and selecting the best results for demonstration. As the graphs in the right column of Fig. 5 show, it was found that the OPTICS algorithm could not completely remove the noise photons.

And it is used a method for determining the denoising parameters of DBSCAN method: during the day, the radius is 1.5 m and at night it is 2.5 m (Ma et al., 2020). It can be seen that DBSCAN's denoising results still include noise but can remove the sparse noise signal (Fig. 7).

3.3. Verification of the extraction accuracy for underwater signal photons

Following the method in step 3 in section 2.3.2, ICESat-2 bathymetry data can be obtained with refraction correction. The denoising effect of the proposed algorithm is evaluated quantitatively by using MAE, RMSE, MRE and R^2 . From Table 3, the range of MAE is 0.54 m-1.57 m. And the range of RMSE is 0.64 m-1.74 m. By comparing MAE and RMSE, they have a similar range of variation. And we can find that the ICESat-2 bathymetry data extracted by the AEDTA algorithm has almost no outliers. Because the chosen waters of the Dongdao Island are much deeper, it has a large MAE but a small MRE. The number of photons reaching the bottom of the water decreases with depth. Due to the large number of noise photons in the 0–2 m water depth range of the Oahu ATL03_20220304 data, the maximum value of the MRE is 20.3 %. In general, the proposed algorithm has good denoising result.

As the graphs in the left column of Fig. 7 show, the ICESat-2 bathymetry data showed approximately the same trend as the *in situ* bathymetry. As the graphs in the right column of Fig. 8 shows, they basically match with the 1:1 line. It is found that the ICESat-2 bathymetry data seems to consistently overestimate the water depth. And this may be related to the setting of the sea surface height and refractive index to constant values.

4. Discussion

4.1. The process for the three times of denoising

According to the algorithm in this paper, only the first one of the two adjacent photons larger than the elevation difference threshold can be

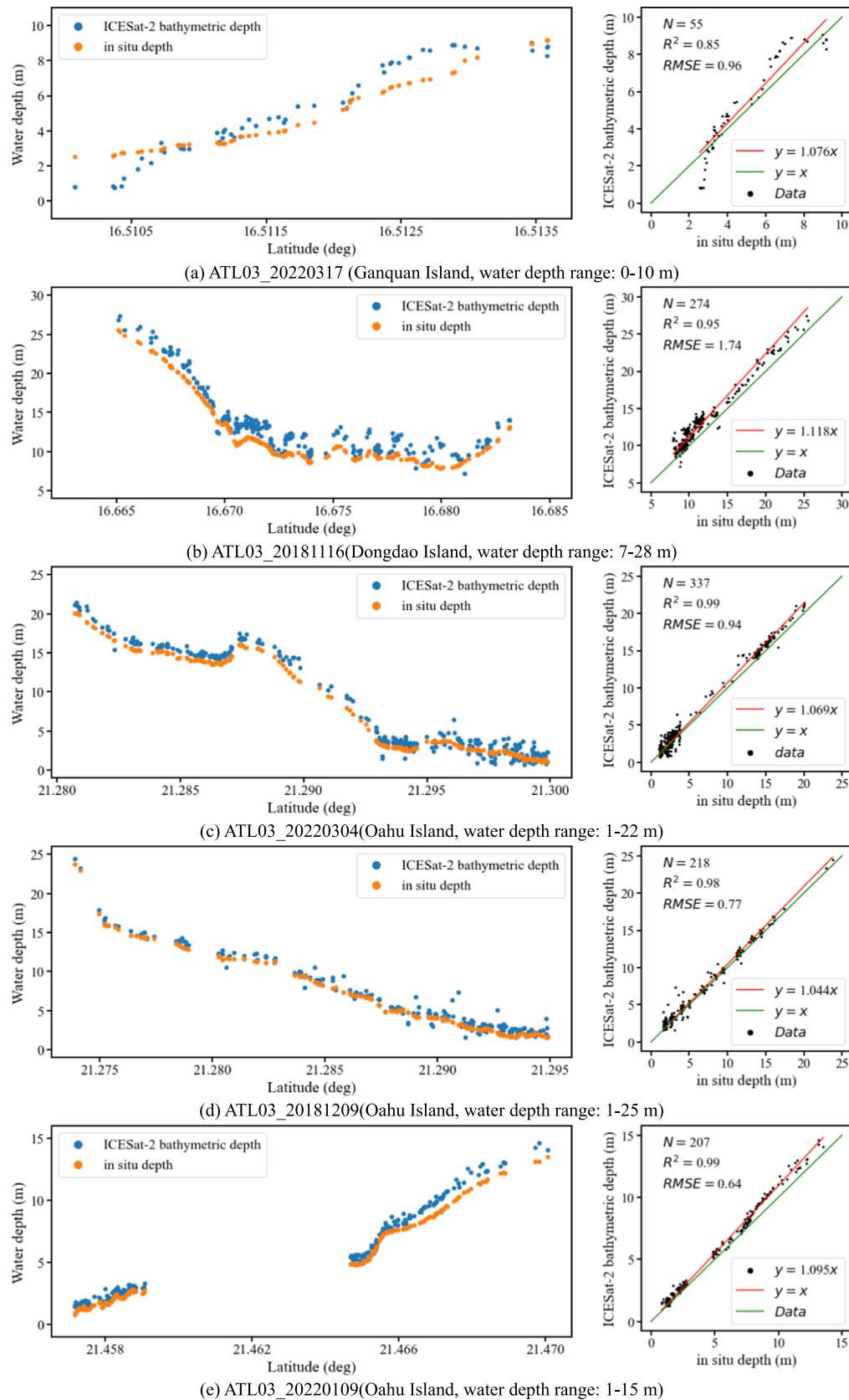


Fig. 8. Comparison of ICESat-2 bathymetry data with *in situ* bathymetry data. The images in the left column show their distribution along the latitude direction. The images in the right column show the deviation of their fitted straight lines from the 1:1 line.

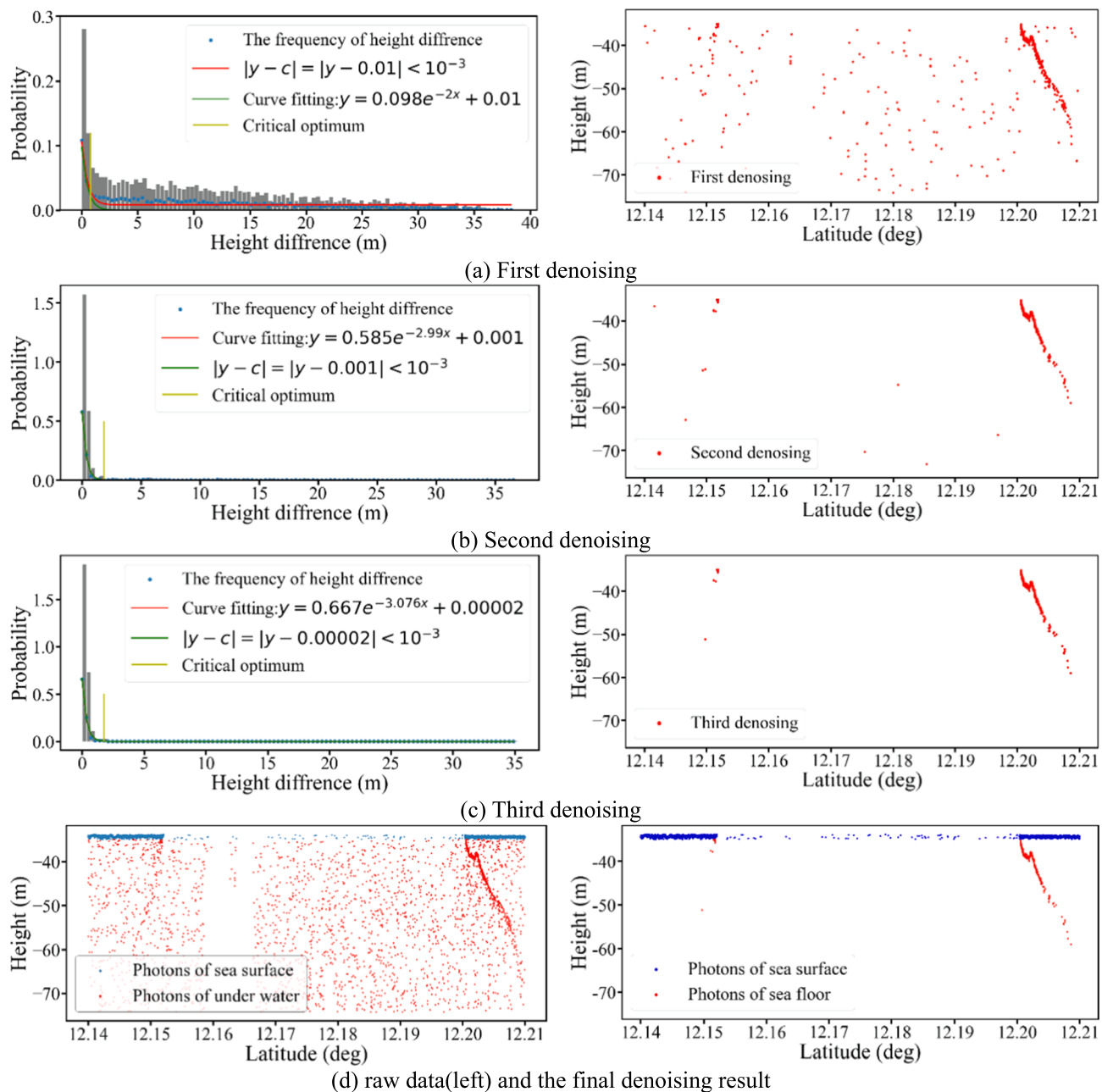


Fig. 9. The process for the three times of denoising with our method. The left column of graphs in (a), (b) and (c) is the elevation difference histogram (gray), the e-exponential fitting (red line), The threshold of optimal elevation difference (yellow line). The right column of graphs in (a), (b) and (c) is the result of each denoising. (d) the raw data (left) and the final denoising result. (For interpretation of the references to color in this figure legend, the reader is referred to the web version of this article.)

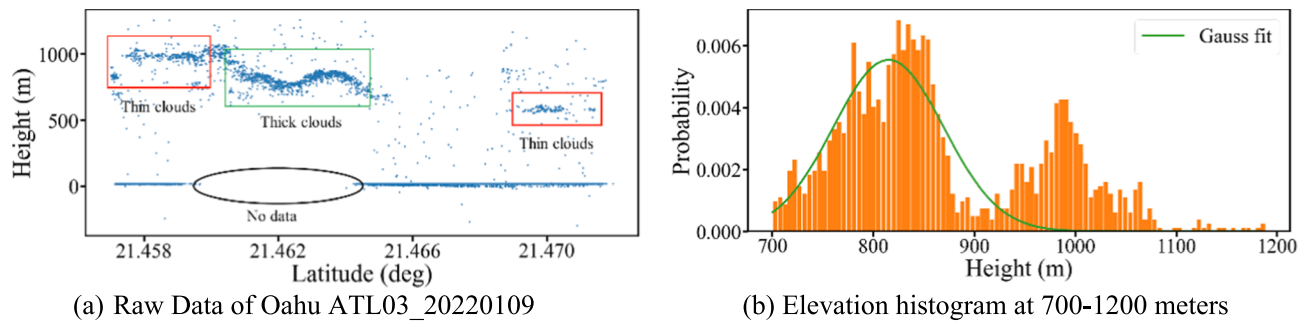
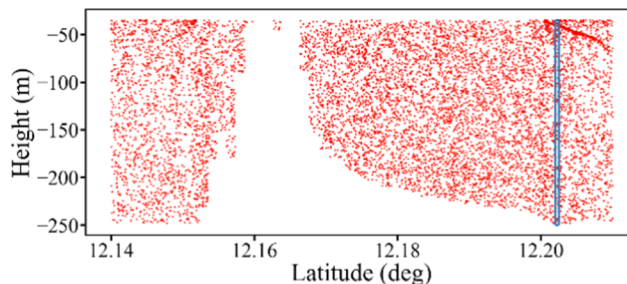
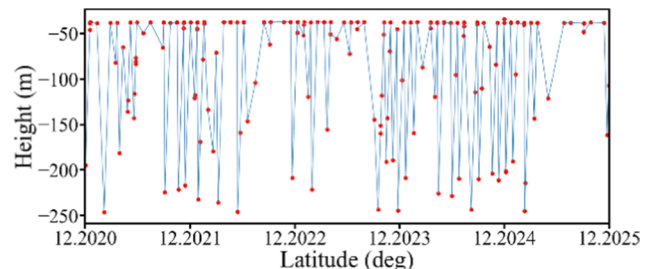


Fig. 10. Gaussian fit analysis of ICESat-2 data with cloud occlusion.



(a) The photons of under water and the name of the data is ATL03_20201019 (Abd al Kuri Island)



(b) The photon of underwater local area (blue box) zoomed in

Fig. 11. Feasibility of elevation difference as a threshold. The red dot is raw data, the blue line is the connection between two adjacent photons. The greater the elevation difference, the greater the possibility of noise photon. (For interpretation of the references to color in this figure legend, the reader is referred to the web version of this article.)

removed in each denoising. Therefore, if the elevation difference between several consecutive photons is very small, such noise cannot be removed by single denoising. In this paper, we use three times denoising to improve the denoising accuracy of our algorithm. Because the along-track sampling interval is 0.7 m and not all photons can penetrate the water surface, the distance along the track of the three adjacent under water photons is greater than or equal to 2.1 m. In this paper, four or more consecutive photons with a small elevation difference are identified as signal photons.

Application of our denoising algorithm to Abd al Kuri Island, which data name is ATL03_2020-10-19 data. Visualize the method of step 2 in section 2.3.2, which is shown in Fig. 9. In Fig. 9 (a)-(c), the amplitude term of the exp-exponential function is getting bigger and bigger, the constant term is getting smaller and smaller, and the number of noise photon is becoming less and less. The Fig. 8(d) shows the raw data and the final denoising results.

4.2. Gaussian fit analysis of ICESat-2 data with cloud occlusion

Multiple Gaussian peaks in the raw photon data due to the presence of clouds, sea surface photons and underwater photons. In Fig. 10, this data has a Gaussian peak at 700–1200 m (green line in Fig. 10 (b)), and the Gaussian peak corresponds to an elevation that is clearly not the sea surface elevation but the cloud layer (red box and green box in Fig. 10 (a)). There is a break in the photons data of sea surface and underwater due to the effect of clouds (black box in Fig. 10(a)). So, we need to first determine the sea surface elevation value based on the elevation

histogram and then filter the photons within 5 m of the sea surface elevation value. A Gaussian fit is then performed on the elevation of the photons in that range to determine the elevation range of the photons at the sea surface. A preliminary screening of photons is necessary before Gaussian fitting.

4.3. Feasibility of elevation difference as a threshold

We selected a small segment of photons (blue box in Fig. 11 (a)) and zoomed in (Fig. 11(b)). By observing Fig. 11(b), it was found that a large difference in elevation between two adjacent photons is more likely to be noise, while it is more likely to be a signal when the difference in elevation between two adjacent photons is small. The idea of AEDTA algorithm is similar to generating DEM with DTM. Select a ground point as the seed point, judge the elevation difference between the subsequent photons and the seed point, mark the points greater than a certain threshold as the ground object points, and the remaining points are the ground points. By analyzing the elevation difference histogram (Fig. 8), we can also find that the elevation difference can be used as a threshold to distinguish signal photons from noise photons.

4.4. Adaptive parameters of the denoising algorithm

According to the feature that the greater the elevation difference between two adjacent photons, the greater the possibility that the photon is noise. We hope that after the selected threshold denoising, the noise photons are less and less, and the signal photons are preserved.

Table 4
Adaptive denoising parameters for photons of underwater.

Location	Denoising times	Fitting of attenuation model	Threshold /m	Noise	Signal
Abd al Kuri Island ATL03 2020-10-19	First denoising	$y = 0.098e^{-2.001x} + 0.0082$	0.77	2220	602
	Second denoising	$y = 0.585e^{-2.995x} + 0.0013$	1.85	150	452
	Third denoising	$y = 0.667e^{-3.076x} + 0.00002$	1.76	25	427
Dongdao Island ATL03 2018-11-16	First denoising	$y = 0.069e^{-1.267x} + 0.0082$	1.50	1710	371
	Second denoising	$y = 0.326e^{-1.496x} + 0.0023$	3.62	80	291
	Third denoising	$y = 0.351e^{-1.501x} + 0.0007$	3.74	13	277
Ganquan Island ATL03 2018-11-16	First denoising	$y = 0.111e^{-1.281x} + 0.0002$	1.86	9	93
	Second denoising	$y = 0.024e^{-4.267x} + 0.0067$	0.73	35	58
	Third denoising	$y = 0.037e^{-1.425x} - 0.0043$	1.59	1	57
Oahu Island ATL03 2022-03-04	First denoising	$y = 0.116e^{-0.542x} + 0.0030$	1.01	905	401
	Second denoising	$y = 0.278e^{-1.418x} + 0.0012$	3.76	36	365
	Third denoising	$y = 0.079e^{-1.586x} + 0.0011$	2.75	26	339
Oahu Island ATL03 2022-01-09	First denoising	$y = 0.304e^{-2.096x} + 0.0039$	0.66	257	216
	Second denoising	$y = 0.389e^{-2.725x} + 0.0002$	2.11	5	211
	Third denoising	$y = 0.392e^{-2.735x} - 0.0003$	2.08	2	207
Oahu Island ATL03 2018-12-09	First denoising	$y = 0.063e^{-0.503x} + 0.0063$	0.75	1807	287
	Second denoising	$y = 0.278e^{-1.688x} + 0.0022$	3.14	55	232
	Third denoising	$y = 0.104e^{-1.506x} + 0.0006$	3.04	12	218

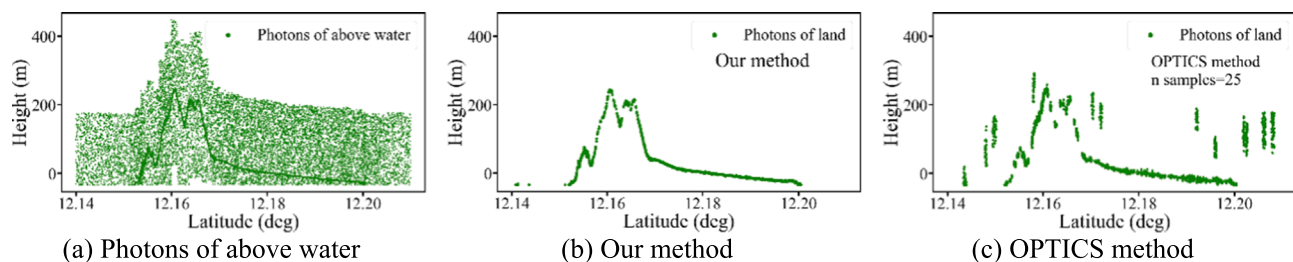


Fig. 12. The denoising results of the algorithm in this paper for terrestrial photons and the comparison with the OPTICS clustering algorithm.

Table 5
Adaptive denoising parameters for photons of land.

Location	Denoising times	Fitting of attenuation model	Threshold /m	Noise	Signal
Abd al Kuri Island ATL03 2020-10-19	First denoising	$y = 0.297e^{-0.512x} + 0.0067$	4.18	17,979	7883
	Second denoising	$y = 0.847e^{-1.106x} + 0.0007$	4.43	623	7260
	Third denoising	$y = 0.833e^{-1.396x} + 0.0003$	3.40	274	6986

Therefore, for the e-exponential fitting of the histogram of the elevation difference, it is hoped that its amplitude term will become larger and larger, and the constant term will become smaller and smaller. And the selected threshold should be able to remove this part of photons with large elevation difference and low frequency. From Table 4, for different research areas, the adaptively selected thresholds achieve the goal of decreasing the proportion of noise and increasing the proportion of signals.

4.5. Denoising effect of land photons

Application of AEDTA method to the denoising of land photons. The raw photon data of land (Fig. 12 (a)) is the ICESat-2 data of Abd al Kuri Island. The denoising result was derived by our method (Fig. 12 (b)) and the denoising result was derived by the OPTICS method (Fig. 12 (c)). The method proposed in this paper has a better detection effect on signal photons of land. But the result denoised by OPTICS method still has a lot of noise.

There are the adaptive denoising parameters for photons of land in Table 5. Compared with the parameters in Table 3, it can be noticed that the selected threshold in land area is significantly larger than the underwater area. This could also explain the necessity of photon classification before denoising.

5. Conclusions

In this paper, a photon denoising algorithm called AEDTA based on adaptive elevation difference thresholding is proposed, which adaptively determines the denoising threshold based on the distribution of elevation differences for different ICESat-2 data. The AEDTA method automatically removes noise and extracts the bathymetric signal from ICESat-2 data. And it greatly reduces the unnecessary time required for manual parameterization, this allows the researcher to devote more effort and time to make further research based on signal photons extracted by our method. The experimental results show that the method in this paper can better detect underwater topography photons compared to the OPTICS and DBSCAN method, and the denoising results have distinguished land, water surface and underwater. After comparison with the *in situ* bathymetry data, the range of MAE is 0.54–1.57 m

and the range of RMSE is 0.64–1.74 m, indicating that most of the photons extracted by the AEDTA algorithm are underwater topographic signal photons. The need for triple denoising and the feasibility of elevation difference as a threshold is demonstrated. And the proposed algorithm also has good results for terrestrial photon denoising. The denoising results of this algorithm for underwater photons can be used as control points for bathymetric inversion mapping.

CRediT authorship contribution statement

Bikang Wang: Conceptualization, Methodology, Software, Visualization, Writing – original draft. **Yi Ma:** Conceptualization, Methodology, Validation, Project administration. **Jingyu Zhang:** Formal analysis, Data curation, Investigation. **Huanwei Zhang:** Resources, Supervision, Writing – review & editing. **Haitian Zhu:** Formal analysis, Investigation. **Zihao Leng:** Supervision, Writing – review & editing. **Xuechun Zhang:** Supervision, Writing – review & editing. **Aijun Cui:** Supervision, Writing – review & editing.

Declaration of Competing Interest

The authors declare that they have no known competing financial interests or personal relationships that could have appeared to influence the work reported in this paper.

Data availability

The authors are unable or have chosen not to specify which data has been used.

Acknowledgments

This work was supported by the National Natural Science Foundation of China (NSFC) [grant numbers 51839002, 41906158]; the Taishan scholar project of Shandong Province [grant number ts20190963]; and the China High Resolution Earth Observation System Program [grant number 41-Y30F07-9001-20/22]. We sincerely thank the Goddard Space Flight Center for distributing the ICESat-2 data (<https://doi.org/10.5067/ATLAS/ATL03.005>), the National Oceanic and Atmospheric Administration (NOAA) for providing the global Relief Model, and the Google Earth Engine (GEE) and European Space Agency (ESA) for distributing the cloud-free composite of the 1-year Sentinel-2 image.

Appendix A

Hardware requirements: PC. RAM:8G.

System requirements: Windows, Linux, Mac.

Program language: Python (3.8).

Dependencies: os, numpy, scipy, pandas and matplotlib modules.

Code and data: <https://github.com/wangbikang/AEDTA>

References

- Albright, A., Glennie, C., 2021. Nearshore bathymetry from fusion of sentinel-2 and ICESat-2 observations. *IEEE Geosci. Remote Sens. Lett.* 18, 900–904. <https://doi.org/10.1109/LGRS.2020.2987778>.
- Babbel, B.J., Parrish, C.E., Magruder, L.A., 2021. ICESat-2 Elevation Retrievals in Support of Satellite-Derived Bathymetry for Global Science Applications. *Geophys. Res. Lett.* 48, e2020G-e90629G. <https://doi.org/10.1029/2020GL090629>.
- Bacalhau, J.R., Ribeiro Neto, A., Crétaux, J., Bergé-Nguyen, M., Moreira, D.M., 2022. Bathymetry of reservoirs using altimetric data associated to optical images. *Adv. Space Res.* 69, 4098–4110. <https://doi.org/10.1016/j.asr.2022.03.011>.
- Caballero, I., Stumpf, R.P., 2019. Retrieval of nearshore bathymetry from Sentinel-2A and 2B satellites in South Florida coastal waters. *Estuarine, Coast. Shelf Sci.* 226, 106277 <https://doi.org/10.1016/j.ecss.2019.106277>.
- Chen, Y., Le, Y., Zhang, D., Wang, Y., Qiu, Z., Wang, L., 2021. A photon-counting LiDAR bathymetric method based on adaptive variable ellipse filtering. *Remote Sens. Environ.* 256, 112326 <https://doi.org/10.1016/j.rse.2021.112326>.
- Costa, B.M., Battista, T.A., Pittman, S.J., 2009. Comparative evaluation of airborne LiDAR and ship-based multibeam SoNAR bathymetry and intensity for mapping coral reef ecosystems[J]. *Remote Sens. of Environ.* 113 (5), 1082–1100. <https://doi.org/10.1016/j.rse.2009.01.015>.
- Ester, M., Kriegel, H.P., Sander, J., Xu, X., 1996. A density-based algorithm for discovering clusters in large spatial databases with noise. *AAAI Press.* 96 (34), 226–231.
- Hsu, H., Huang, C., Jasinski, M., Li, Y., Gao, H., Yamanokuchi, T., Wang, C., Chang, T., Ren, H., Kuo, C., Tseng, K., 2021. A semi-empirical scheme for bathymetric mapping in shallow water by ICESat-2 and Sentinel-2: A case study in the South China Sea. *ISPRS J. Photogramm. Remote Sens.* 178, 1–19. <https://doi.org/10.1016/j.isprsjprs.2021.05.012>.
- Li, Y., Gao, H., Jasinski, M.F., Zhang, S., Stoll, J.D., 2019. Deriving High-Resolution Reservoir Bathymetry From ICESat-2 Prototype Photon-Counting Lidar and Landsat Imagery. *IEEE Trans. Geosci. Remote Sens.* 57, 7883–7893. <https://doi.org/10.1109/TGRS.2019.2917012>.
- Lin, X., Xu, M., Cao, C., Dang, Y., Huang, Z., 2020. Estimates of Forest Canopy Height Using a Combination of ICESat-2/ATLAS Data and Stereo-Photogrammetry. *Remote Sens.* 12, 21.
- Ma, Y., Xu, N., Liu, Z., Yang, B., Yang, F., Wang, X.H., Li, S., 2020. Satellite-derived bathymetry using the ICESat-2 lidar and Sentinel-2 imagery datasets. *Remote Sens. Environ.* 250, 112047 <https://doi.org/10.1016/j.rse.2020.112047>.
- Magruder, L.A., Brunt, K.M., 2018. Performance Analysis of Airborne Photon-Counting Lidar Data in Preparation for the ICESat-2 Mission. *IEEE Trans. Geosci. Remote Sens.* 56, 2911–2918. <https://doi.org/10.1109/TGRS.2017.2786659>.
- Markus, T., Neumann, T., Martino, A., Abdalati, W., Brunt, K., Csatho, B., Farrell, S., Fricker, H., Gardner, A., Harding, D., Jasinski, M., Kwok, R., Magruder, L., Lubin, D., Luthcke, S., Morison, J., Nelson, R., Neuenschwander, A., Palm, S., Popescu, S., Shum, C.K., Schutz, B.E., Smith, B., Yang, Y., Zwally, J., 2017. The Ice, Cloud, and Land Elevation Satellite-2 (ICESat-2): Science requirements, concept, and implementation. *Remote Sens. Environ.* 190, 260–273. <https://doi.org/10.1016/j.rse.2016.12.029>.
- Neuenschwander, A., Katherine, P., 2018. Algorithm Theoretical Basis Document (ATBD) for Land-V egation Along-Track Products(ATL08). *e-Convers.-Propos. Clust. Excell.* 2, 1–140.
- Parrish, C.E., Magruder, L.A., Neuenschwander, A.L., Forfinski-Sarkozy, N., Alonso, M., Jasinski, M., 2019. Validation of ICESat-2 ATLAS Bathymetry and Analysis of ATLAS's Bathymetric Mapping Performance. *Remote Sens.* 11, 1634. <https://doi.org/10.3390/rs11141634>.
- Pedregosa, F., Varoquaux, G., Gramfort, A., Michel, V., Thirion, B., Grisel, O., Blondel, M., Prettenhofer, P., Weiss, R., Dubourg, V., 2011. Scikit-learn: Machine Learning in Python. *JMLR.org* 12, 2825–2830.
- Ranndal, H., Siggaard Christiansen, P., Kliving, P., Baltazar Andersen, O., Nielsen, K., 2021. Evaluation of a Statistical Approach for Extracting Shallow Water Bathymetry Signals from ICESat-2 ATL03 Photon Data. *Remote Sens.* 13, 3548. <https://doi.org/10.3390/rs13173548>.
- Suriseddy, V.V.A.K., Rajput, P., Ramakrishnan, R., Venkateswarlu, C., 2022. Synergistic Fusion of ICESat-2 Lidar and Sentinel-2 Data to Leverage Potential Mapping of Bathymetry in Remote Islands Using SVR. *J. Indian Soc. Remote Sens.* 50, 1–9. <https://doi.org/10.1007/s12524-022-01537-4>.
- Thomas, N., Pertwi, A.P., Tragano, D., Lagomasino, D., Poursanidis, D., Moreno, S., Fatoyinbo, L., 2021. Space-Borne Cloud-Native Satellite-Derived Bathymetry (SDB) Models Using ICESat-2 And Sentinel-2. *Geophys. Res. Lett.* 48, e2020G-e92170G. <https://doi.org/10.1029/2020GL092170>.
- Thomas, N., Lee, B., Coutts, O., Bunting, P., Lagomasino, D., Fatoyinbo, L., 2022. A Purely Spaceborne Open Source Approach for Regional Bathymetry Mapping. *IEEE Trans. Geosci. Remote Sens.* 60, 1–9. <https://doi.org/10.1109/TGRS.2022.3192825>.
- Wang, Y., Yang, X., Wang, C., 2022. Vegetation and land classification method based on the background noise rate of a photon-counting LiDAR. *Opt. Express* 30, 14121. <https://doi.org/10.1364/OE.456447>.
- Xie, C., Chen, P., Pan, D., Zhong, C., Zhang, Z., 2021a. Improved Filtering of ICESat-2 Lidar Data for Nearshore Bathymetry Estimation Using Sentinel-2 Imagery. *Remote Sens.* 13, 4303. <https://doi.org/10.3390/rs13214303>.
- Xie, H., Xu, Q., Ye, D., Jia, J., Sun, Y., Huang, P., Li, M., Liu, S., Xie, F., Hao, X., Tong, X., 2021b. A Comparison and Review of Surface Detection Methods Using MBL, MABEL, and ICESat-2 Photon-Counting Laser Altimetry Data. *IEEE J Sel. Top. Appl. Earth Obs. Remote Sens.* 14, 7604–7623. <https://doi.org/10.1109/JSTARS.2021.3094195>.
- Xie, H., Ye, D., Xu, Q., Sun, Y., Huang, P., Tong, X., Guo, Y., Liu, X., Liu, S., 2022. A Density-Based Adaptive Ground and Canopy Detecting Method for ICESat-2 Photon-Counting Data. *IEEE Trans. Geosci. Remote Sens.* 60, 1–13. <https://doi.org/10.1109/TGRS.2022.3176982>.
- Xu, N., Ma, Y., Zhou, H., Zhang, Z., Wang, X.H., 2022. A Method to Derive Bathymetry for Dynamic Water Bodies Using ICESat-2 and GSWD Data Sets. *IEEE Geosci. Remote Sens. Lett.* 19, 1–5. <https://doi.org/10.1109/LGRS.2020.3019396>.
- Yang, P., Fu, H., Zhu, J., Li, Y., Wang, C., 2022. An Elliptical Distance Based Photon Point Cloud Filtering Method in Forest Area. *IEEE Geosci. Remote Sens. Lett.* 19, 1–5. <https://doi.org/10.1109/LGRS.2021.3124612>.
- NASA. 15 October 2019. "ICE, CLOUD, and Land Elevation Satellite (Icesat-2) Algorithm Theoretical Basis Document (ATBD) for Global Geolocated Photons (ATL03)". ICESat-2 website. Accessed on 20 November 2019. https://icesat-2.gsfc.nasa.gov/sites/default/files/page_files/ICESat2_ATL03_ATBD_r002.pdf.
- Yi, M.A., Zhang, J., Zhang, J.Y., Zhang, Z., Wang, J.J., 2018. Progress in Shallow Water Depth Mapping From Optical Remote Sensing. *Adv. Mar. Sci.* 36, 331–351. <https://doi.org/CNKI:SUN:HBHH.2018-03-001>.
- Zhang, X., Chen, Y., Le, Y., Zhang, D., Yan, Q., Dong, Y., Han, W., Wang, L., 2022. Nearshore Bathymetry Based on ICESat-2 and Multispectral Images: Comparison Between Sentinel-2, Landsat-8, and Testing Gaofen-2. *IEEE J. Sel. Top. Appl. Earth Obs. Remote Sens.* 15, 2449–2462. <https://doi.org/10.1109/JSTARS.2022.3153681>.
- Zhang, D., Chen, Y., Le, Y., Dong, Y., Dai, G., Wang, L., 2022a. Refraction and coordinate correction with the JONSWAP model for ICESat-2 bathymetry. *ISPRS J. Photogramm. Remote Sens.* 186, 285–300. <https://doi.org/10.1016/j.isprsjprs.2022.02.020>.
- Zhang, W., Xu, N., Ma, Y., Yang, B., Zhang, Z., Wang, X.H., Li, S., 2021. A maximum bathymetric depth model to simulate satellite photon-counting lidar performance. *ISPRS J. Photogramm. Remote Sens.* 174, 182–197. <https://doi.org/10.1016/j.isprsjprs.2021.02.013>.
- Zhu, X., Nie, S., Wang, C., Xi, X., Wang, J., Li, D., Zhou, H., 2021. A noise removal algorithm based on OPTICS for Photon-Counting LiDAR Data. *IEEE Geosci. Remote Sens. Lett.* 18, 1471–1475. <https://doi.org/10.1109/LGRS.2020.3003191>.

Further reading

- Ankerst, M., Breunig, M.M., Kriegel, H.P., Sander, J., 1999. OPTICS: Ordering Points to Identify the Clustering Structure. In: SIGMOD 1999, Proceedings ACM SIGMOD International Conference on Management of Data, June 1–3, 1999, Philadelphia, Pennsylvania, USA. <https://dl.acm.org/doi/10.1145/304182.304187>.
- Neumann, T.A., Brenner, A., Hancock, D., Robbins, J., Saba, J., Harbeck, K., Gibbons, A., Lee, J., Lutheke, S.B., Rebold, T., et al., 2021. ATLAS/ICESat-2 L2A Global Geolocated Photon Data, Version 5. NASA National Snow and Ice Data Center Distributed Active Archive Center, Boulder, Colorado USA.